

ARTICLE OPEN



Effect of decades of corrosion on the microstructure of altered glasses and their radiation stability

Anamul Haq Mir¹✉, Amreen Jan², Jean-Marc Delaye², Stephen Donnelly¹ , Jonathan Hinks¹ and Stephane Gin²

Understanding the microstructural evolution of glasses during their interaction with water and radiation is of fundamental importance in addressing the corrosion of nuclear waste forms under geological disposal conditions. Here we report the results of more than 21 years of corrosion of two borosilicate glasses showing the formation of mesoporous C–S–H gels in Ca-bearing glasses and a mainly microporous microstructure in Al-bearing glasses. These porous corroded glasses were then irradiated with heavy ions to simulate the effects of recoil nucleus damage and monitored in real time using transmission electron microscopy with in situ ion irradiation. The ballistic collisions remarkably healed the porous corroded glasses to a pore-free homogeneous microstructure. Besides providing new insights and predictions about how doped glasses and actual waste forms may evolve under corrosion and irradiation, the results highlight the non-universal nature of the existing corrosion models and the important role that the glass composition and radiation damage play in the evolution of the microstructure during corrosion.

npj Materials Degradation (2020)4:11; <https://doi.org/10.1038/s41529-020-0115-0>

INTRODUCTION

The basic mechanisms of glass corrosion are still not very well established, and two fundamentally different models have gained significant attention in the last few years. According to the first model^{1–3}, selective ion exchange of alkali with H⁺/H₃O⁺ (inter-diffusion) and subsequent structural reorganisation of the hydrated glass leads to the formation of a silica-rich surface alteration layer (SAL) that tends to slow down the rate of glass corrosion. The second model^{4–6} proposes that the SAL is formed as a result of simultaneous glass dissolution and silica precipitation from a thin layer of supersaturated water present at the glass–water interface. Evidence in favour of both of these models^{3,6–9} shows that they are non-universal in nature, and attempts of developing unifying models have been made¹⁰. Nevertheless, none of these models directly take into account the effect of glass composition¹¹ and leaching conditions on the microstructure of the leached glass and the impact of this microstructure on mass transport. Empirical kinetic models such as GRAAL (glass reactivity with allowance for the alteration layer) or GM2001 (Grambow, Muller) include fitting parameters to account for these effects¹². To develop any universal or unifying predictive model accounting for the interplay of various corrosion mechanisms such as inter-diffusion, hydrolysis, condensation and precipitation, the nanoscale microstructure of the altered glasses needs to be better understood because it ultimately controls the transport of water and the glass constituents. Deciphering the mechanisms of glass corrosion and microstructure of the corroded glasses is key to addressing the release and transport of radioelements from nuclear waste glasses under disposal conditions^{13,14}. In addition, nuclear waste glasses will also suffer self-irradiation damage from the decay of the confined radioelements. The effects of self-irradiation damage on the microstructure of corroded glasses are still poorly understood. Addressing whether such irradiation effects can play a role in the mass transport through the alteration layer and in the corrosion of the actual waste packages remains an enigma¹⁵. Deconvoluting the effects of self-irradiation damage on the microstructure is key

to addressing the compatibility of the short-term corrosion tests performed on highly radioactive (doped specimens) and non-active specimens, and to correctly forecast the behaviour of mildly radioactive nuclear waste glasses after thousands of years of disposal.

In this study, two different glass powders corroded for about 21.6 years (in static mode, at 90 °C. See “Methods” for details) were analysed using multiple characterisation techniques to understand their corrosion and microstructural evolution. Both the glasses contained SiO₂, B₂O₃ and Na₂O but, in addition, one of them contained CaO (CJ8 glass), whereas the other one contained Al₂O₃ instead (CJ2 glass), allowing decoupling of the effects of a network former (Al) and network modifier (Ca) on their dissolution and microstructure. Owing to this compositional difference, CJ8 is more depolymerised and has a higher propensity to hydrolyse than the CJ2 glass¹⁶. Alteration of these two glasses was monitored using ICP-OES over the years; the microstructure was studied using scanning and transmission electron microscopies (SEM and TEM). Also, short-term leaching (as detailed in the Methods) with isotope tracing (²⁹Si and ¹⁸O) and time-of-flight secondary ion mass spectroscopy (ToF-SIMS) were employed to study the SAL formation and diffusion/transport. The corroded glasses (21-year corroded glass) were then subjected to heavy-ion irradiation to simulate the effects of self-irradiation damage on their microstructure using TEM with in situ ion irradiation. These short- and long-term corrosion tests coupled with their irradiation stability allowed us to investigate the applicability of the aforementioned corrosion models and predict the implications of self-irradiation damage on the microstructure of doped glasses and the actual nuclear waste forms.

RESULTS AND DISCUSSION

Effect of corrosion on the microstructure

The concentration of various elements in the solution monitored over 21.6 years is shown in Fig. 1 in the Supplementary

¹Electron Microscopy and Materials Analysis, School of Computing and Engineering, University of Huddersfield, Queensgate HD1 3DH, UK. ²CEA, DEN, Service d'études de vitrification et procédés hautes températures, 30207 Bagnols-sur-Ceze, France. ✉email: a.h.mir@hud.ac.uk

Information. Based on the boron release, the CJ8 glass was fully altered after about 6000 days, whereas the CJ2 glass was 63% altered by the end of the experiment (7876 days). SEM and bright-field TEM images (BF-TEM) of the corroded CJ8 glass at low and high magnification are shown in Figure 1a–h. Figure 1a shows a low-magnification SEM image of one of the corroded particles highlighting its rough morphology. Magnified images of the regions indicated by the rectangles are shown in Fig. 1b, c showing that the microstructure is highly porous. Figure 1d shows a magnified region from a different particle to highlight the different kinds of porous morphologies typically observed in the SEM. Figure 1e shows a low-magnification BF-TEM image of the focus ion beam (FIB)-milled lamellae. It clearly shows that the microstructure consists of a very high degree of porosity and an interwoven fibrillar network as indicated by the SEM images. Interestingly, this is very similar to the microstructures of calcium–silicate–hydrate (C–S–H) gels found in a diverse range of cementitious materials such as Portland cement^{17,18}. However, the phases found here are formed at a much lower pH. Figure 1f–h shows higher-magnification images in different regions of this C–S–H gel to highlight the regions of large pores and low density of fibrils (in Fig. 1f), intermediate pore size and fibril density (in Fig. 1g) and high fibril density and small pores (in Fig. 1h). The average fibril diameter obtained from the measurements of 61 fibrils was 5 ± 0.2 nm (see Fig. 2 in the Supplementary Information for the distribution and further description on the fibrils). Electron energy-loss spectra (EELS) captured in the C–S–H gel confirmed the presence of Ca, Si and O (Fig. 3 in the Supplementary Information), and TEM diffractograms taken from various regions of the TEM lamella showed the gel to be amorphous. In addition to the FIB lamellae, the leached powders were further crushed using an agate mortar and pestle to obtain thin flakes/particles for TEM analysis. Their analysis also confirmed the presence of the C–S–H gel and its amorphous nature. However, certain gel particles also showed the presence of a very small percentage of crystals of a few nanometres in size, indicating the presence of other secondary crystalline phases. The crystals measured no more than the diameter of the fibrils in their longest direction. Bright- and dark-field images, TEM diffractograms and EELS spectra of these crushed powders are shown in Fig. 4 in the Supplementary Information, and are consistent with what was observed on the FIB lamellae. The presence of Ca in the CJ8 glass therefore clearly favoured the formation of a typical C–S–H gel microstructure commonly referred to as “nanofoil” morphology and usually found in synthetic C–S–H and Portland cement systems with high alkaline content ($\text{Ca}:\text{Si} > 1$)¹⁸. In the cements, the microstructure of the C–S–H gels is usually classified into inner-product/high-density (Ip) and outer-product/low-density (Op), depending on whether the C–S–H gel occupies the volume of the original grain (Ip) or the originally water-filled spaces (Op)^{17,19}. The Op C–S–H is known to have a directional fibrillar structure with a 3D-interconnected network of pores occupying the spaces between the fibrils (referred to as capillary porosity). The directional fibrillar structure is clearly evident in Fig. 1 and in many other figures shown in the Supplementary Information, lending support to the assertion that the CJ8 microstructure, in this case, is consistent with a low-density C–S–H gel. In fact, these images are indistinguishable from the low-density C–S–H gels found by Richardson in his seminal work on hardened white Portland cement (see figures 15–17 in ref. 17).

The SEM and BF-TEM images of the corroded CJ2 glass are shown in Fig. 2a–f. Figure 2a–c shows low- and high-magnification SEM images highlighting the presence of a porous discontinuous layer on the corroded particles (indicated in Fig. 2c). Based on the morphology, this layer will be referred to as a precipitated layer. The thickness of the precipitated layer varied between particles and also between locations on individual particles (additional images are shown in Fig. 1b in the Supplementary Information). A

magnified image of the cracked region indicated by the small rectangle in Fig. 2a is shown in Fig. 2d indicating the width of the precipitated layer to be about 180 nm. BF-TEM images of the FIB lamellae are shown in Fig. 2e, f. Beneath the protective carbon and chromium layers as shown in Fig. 2e (deposited prior to TEM lamellae preparation), there is a rough mesoporous layer (MeL) containing large pores, which is followed by an inner microporous layer (MiL) of the altered glass (hereafter referred to as gel). The width of the MeL varied from ~ 60 nm to ~ 420 nm amongst the analysed specimens (Fig. 1a in the Supplementary Information), which is consistent with the observations made on the SEM images. A magnified image of the inner MiL is shown in Fig. 2f and the inset highlights the typical pores found in this layer (bright spots). The size distribution of the pores in the MiL is shown superimposed on Fig. 2e (more discussion on the measurement of pores is presented in section 4 in the Supplementary Information). The pores followed a log-normal trend (white dashes) with a mean pore diameter of 0.8 ± 0.2 nm. The areal density of the pores (pores per unit projected area) was found to be $5.5 \times 10^{11} \text{ cm}^{-2}$ ($\pm 20\%$). The projected areal density as such cannot be translated into volumetric density because the overlapping pores are not accounted for, but it provides a reasonable way of relative comparison between the specimens of similar thicknesses. Given the thickness of the specimen (~ 100 nm) and the size of the pores, especially in the CJ2 glass, multiple overlapping pores can appear as a single pore of a size that can be different from the individual overlapping pores. This pore overlap can potentially skew the actual pore-size distribution, and therefore the effects of specimen thickness on the pore-size distribution need to be deconvoluted. This will be addressed in a separate publication in the near future (see also section 4 in the Supplementary Information for additional information). Nonetheless, it is worth mentioning that semi-quantitative results obtained using spectroscopic ellipsometry and Kelvin equation indicate pore sizes that essentially lie within the limits of the pore-size distribution shown here although it was not possible to precisely evaluate the size distribution in that study²⁰.

The field of view for the TEM images ranged from about 2–3 μm depending on the specimen, and the entire field of view was found to be microporous (MiL). This indicated that the altered depth was greater than 3 μm , which is in good agreement with the estimates of the alteration thickness obtained from the leaching data (~ 3 –4 μm based on the B concentration given in Fig. 2 in the Supplementary Information). TEM diffractograms from different regions of the lamellae showed the gel to be amorphous. These results show that the microstructure of the corroded CJ2 glass consists of a thin precipitated mesoporous surface layer encapsulating the inner microporous altered glass.

To better understand how SALs form on these two glasses, small monoliths of the CJ8 and CJ2 glasses were leached for 33 days at 90 °C and pH 9 in silica-saturated solution (highly enriched in ²⁹Si) and then characterised using ToF-SIMS after the leaching. The ToF-SIMS profiles are shown in Fig. 3a, b for the CJ8 and CJ2 glasses, respectively. The CJ8 glass showed an outer layer of ~ 600 nm composed of C–S–H only and a thick layer composed of both the C–S–H and the glass (referred to hereafter as mixed layers (ML)). This layer results in a known artefact of ToF-SIMS depth profiling that appears when the analysis is performed on a porous/rough material made of non-uniform layers leading to gradual intensity changes and apparent enlargement of the otherwise sharp planar interfaces/alteration front²¹. The C–S–H layer is depleted in B and Na, and displays a large increase in the ²⁹Si/²⁸Si ratio relative to the pristine glass. Besides, the ²⁹Si/²⁸Si ratio in the solution dropped from 79 in the onset solution to 1.5 at the end of the experiment, whereas the total Si concentration remained constant. Altogether, these data on Si show that the glass supplied the solution with ²⁸Si and the dissolved Si precipitated from the bulk solution to form the C–S–H phases.

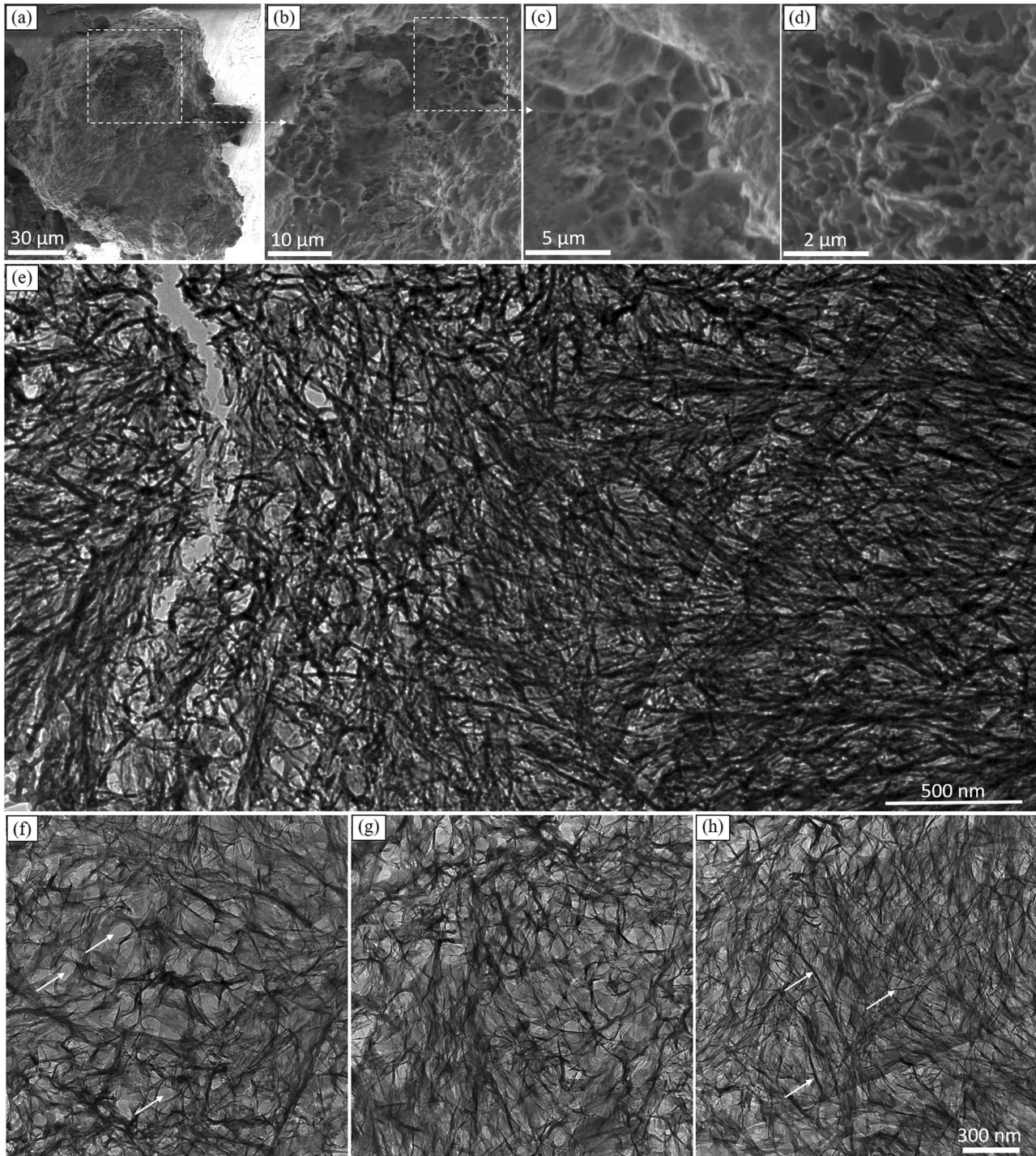


Fig. 1 SEM and BF-TEM images of the corroded CJ8 glass powder ($t_{\text{leach}} = 7291$ days, $T = 90$ °C, $\text{pH}^{\text{@}90} = 9$). **a** A low-magnification SEM image of a corroded CJ8 particle. **b**, **c** Magnified images of the regions indicated by the rectangles highlighting the presence of a porous microstructure. **d** A magnified image from a different particle to show the typical microstructures observed in the SEM images. **e** A low-magnification TEM image to give an overview of the C-S-H gel formed upon corrosion, and **f–h** higher-magnification images in different regions of the gel layer highlighting the porosity and the interconnected ligaments/fibrils with low, medium and high fibril density in going from left to right. The arrows in **(f)** indicate the typical pores and the arrows in **(h)** indicate the typical ligaments. Image defocus (d_f) ~ 4 μm under focus for **(e)** and ~ 2 μm under focus for **f–h**. The scale marker in **(h)** also applies to **(f)** and **(g)**.

Therefore, an interface-coupled dissolution–reprecipitation model can correctly describe the corrosion of the CJ8 glass. In the case of the CJ2 glass, the ToF-SIMS profiles confirmed the absence of B in the gel and partial retention of Na, which likely charge-compensate Al units. Contrary to CJ8, $^{29}\text{Si}/^{28}\text{Si}$ in the gel remained the same as in the pristine glass, indicating that the gel is formed

with Si atoms of the glass. Only the outermost layer (P layer) displayed a thin zone of ~ 10 -nm thickness significantly enriched in ^{29}Si ($^{29}\text{Si}/^{28}\text{Si}$ up to 0.4) (Fig. 3b, inset). This zone might correspond to a precipitate formed on the gel surface. Solution data indicate a decrease in $^{29}\text{Si}/^{28}\text{Si}$ from 79 to 44 at the end of the experiment. This drop corresponds to an equivalent thickness of

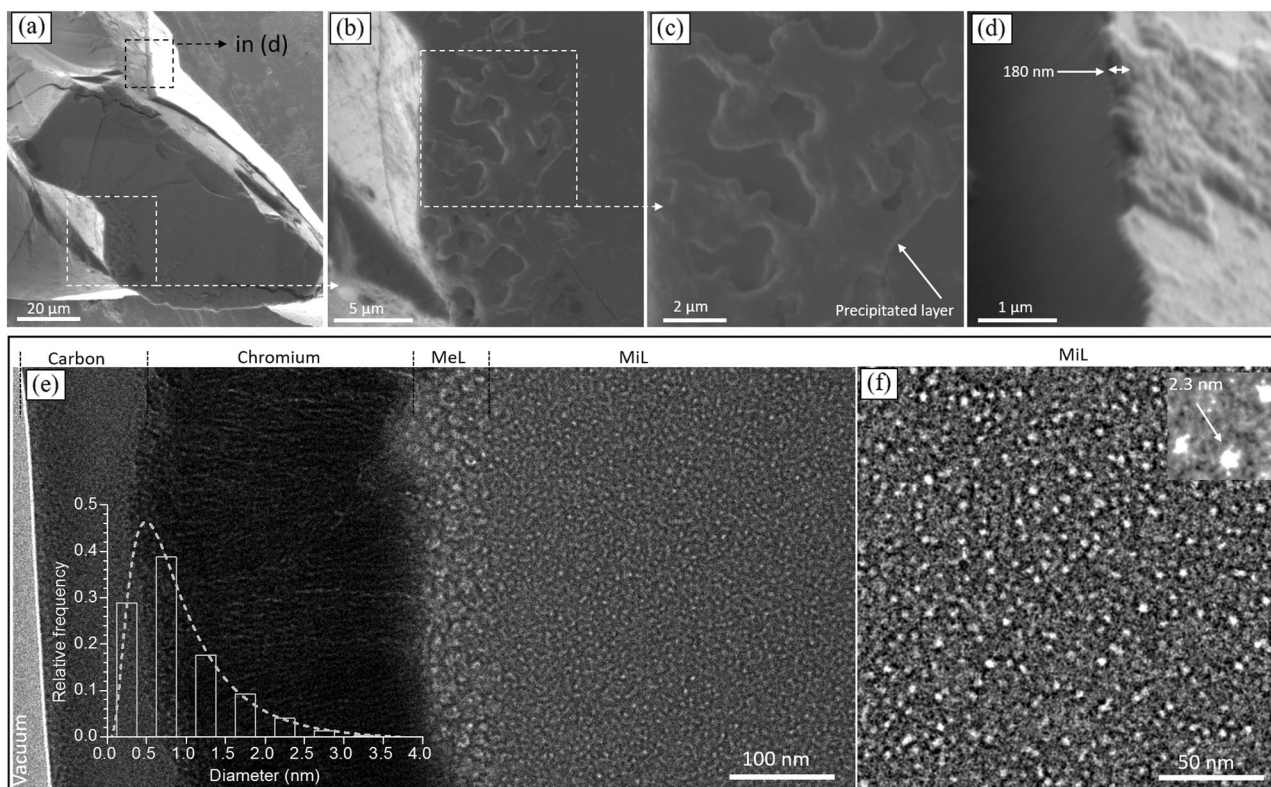


Fig. 2 SEM and BF-TEM images of the corroded CJ2 glass powder ($t_{\text{leach}} = 7876$ days, $T = 90^\circ\text{C}$, $\text{pH}^{90} = 9$). **a–c** Low- and high-magnification SEM images showing the presence of a spatially inhomogeneous precipitated layer. **d** A magnified image of the cracked region indicated by the small rectangle in **(a)** (the precipitated layer measured about 180 nm in thickness). **e** BF-TEM image of a FIB lamellae. The protective carbon and chromium were deposited before making the TEM lamella to prevent any surface damage to the thin precipitated layer. The microstructure consists of an outer mesoporous layer (MeL) followed by an inner microporous layer (MiL). The frequency distribution of the pores in the MiL and their log-normal fit ($R\text{-square} > 0.98$) is shown superimposed (the number of analysed pores = 9445). **f** A higher-magnification BF-TEM image in the MiL to better visualise the pores. The inset highlights the typical pores. $D_f \sim 4 \mu\text{m}$ under focus.

~ 8 nm of silica in reasonable agreement with ToF-SIMS analysis. The alteration of the CJ2 glass is thus made of a thin outermost layer that has exchanged a large amount of Si with the solution, and a large homogeneous gel formed with no Si exchange with the solution. These results are in excellent agreement with the microstructure observed for the CJ2 glass. Both the long-term and short-term corrosion experiments show that the microstructural evolution in the CJ2 glass is dominated by the internal structural reorganisation of the hydrated and lower-density aluminosilicate skeleton, leading to the formation of pores through condensation reactions of silanol groups². The stability provided by Al is firstly due to the higher strength of the Si–O–Al bonds in comparison with the Si–O–Si bonds, and secondly due to the relatively higher degree of polymerisation of the CJ2 glass. Both these factors help to reduce the hydrolysis and dissolution of the aluminosilicate glass network. Thus, we eventually end up with two different glass compositions essentially following different corrosion mechanisms (one mechanism dominating over the other depending on the composition) resulting in entirely different microstructures. It is plausible to propose that hydrolysis and reprecipitation dominate over condensation and internal reorganisation in the case of the CJ8, whereas the opposite is true for the CJ2 glass.

Effect of heavy-ion irradiation on the microstructure

To evaluate the radiation stability of the corroded glasses, the specimens of CJ8 and CJ2 were irradiated with 640- and 600-keV Xe ions at -130°C using a TEM with in situ ion irradiation. The ion energies were chosen to avoid any implantation in the thin FIB lamellae ($\sim 100\text{-nm}$ thick), and the Xe ions were used due to their

inert nature. Successive images taken after a time interval of 2–3 min of ion irradiation are shown in Fig. 4 for the CJ8 and in Fig. 5 for the CJ2 glass. In the CJ8 glass, the majority of the pores were observed to shrink and finally close due to ion irradiation, resulting in the formation of a uniform specimen without any pores or ligaments in most of the gel layer after about $1.4 \times 10^{15} \text{Xe.cm}^{-2}$. Similar effects were observed in the CJ2 glass. All the pores shrunk in size and were completely closed when a fluence of $4.6 \times 10^{14} \text{Xe.cm}^{-2}$ was reached. The majority of the cavities were, however, already closed at a fluence of about $3.4 \times 10^{14} \text{ions.cm}^{-2}$, and cavities that were initially less than 1 nm in diameter were completely closed after $2.3 \times 10^{14} \text{ions.cm}^{-2}$.

From several experimental studies and atomistic simulations^{22–24}, it is now reasonably well understood that the internal pressure of the cavities plays an important role in their stability under ion irradiation. Ballistic collisions displace the target atoms and induce a mass flow towards the regions of low internal pressure. This mass flow continues until a balance between internal pressure and surface tension is established. In the case of empty cavities, the internal pressure is zero, and therefore, the mass flow continues unrestrained, resulting in the shrinkage and eventual closure of the cavities. The overall effect of ballistic collisions is (essentially) to redistribute mass from the regions of high density towards the regions of low density. Focusing on the behaviour of the cavities/pores ≤ 1 nm in diameter, the results on the CJ2 showed that it took only $\sim 2.3 \text{ions.nm}^{-2}$ for pore closure. This translates into about four ion impacts per cubic nanometre of the pore volume required to completely close it. Pores with a diameter of ~ 0.8 nm (the mean of the distribution) or less would then require only a single-ion impact for their closure. Essentially,

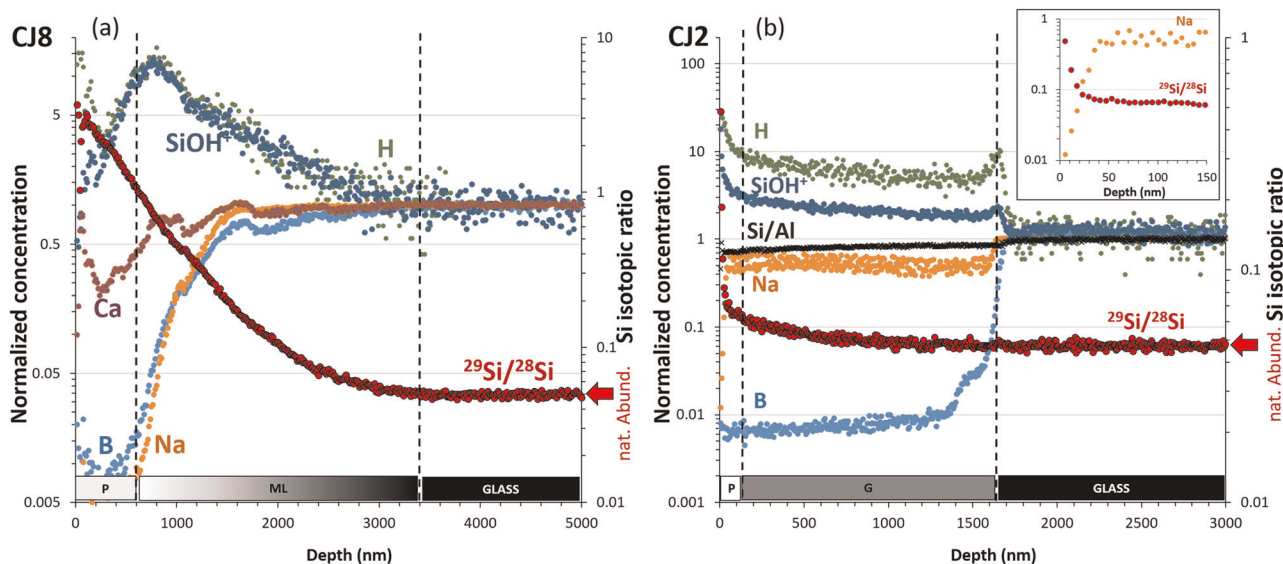


Fig. 3 ToF-SIMS profiles of CJ8 and CJ2 glass coupons leached for 33 days ($T = 90\text{ }^{\circ}\text{C}$, $\text{pH}^{90\text{ }^{\circ}\text{C}} \text{ } 9$) in a solution enriched with ^{29}Si . **a** Depth profiles for CJ8 showing B, H, Al, Na, Ca and $^{29}\text{Si}/^{28}\text{Si}$ ratio (right axis), and **b** depth profiles for CJ2 showing B, Al, H, Na, Ca and $^{29}\text{Si}/^{28}\text{Si}$ ratio (right axis). The inset highlights the profiles in the near-surface region. P stands for precipitated layer only, ML for mixed layers and G for gel.

these results show that the majority of the cavities would require a single-ion impact to completely close them. Irradiation-induced closure of cavities can potentially lead to sealing or constraining the pathways for the transport of water and radioelements through SALs. The question as to how much of a role this can play in the real waste packages is still an open one, and a discussion on the subject is provided later within the context of the behaviour of bubbles and voids to ballistic collisions.

Nevertheless, significant insights can already be obtained from the results available thus far. A reasonable way of comparing a typical 100-keV recoil nucleus with the Xe ions used in this study is to compare its displacement damage levels as shown in Fig. 6. A 100-keV recoil nucleus (U atom in this case) on average creates ~ 36 displacements per nm along its path (range ~ 40 nm), whereas 600-keV Xe ions along their path in a 100-nm-thick TEM specimen on average create only ~ 23 displacements. Considering that a single Xe ion impact is needed to close the cavities of about 1 nm in diameter, the heavier recoil nuclei, which create a greater damage level (by $\sim 60\%$), are therefore more than capable of completely closing such a cavity in a single impact. Studies of irradiation-induced density changes using molecular dynamics and actinide doping have shown that recoil nuclei on average create a damage volume of about 300 nm^3 (see refs. ^{25,26}). Using this value of damage volume, it is possible to consider the potential implications of the presence of radioelements on the evolution of the microstructure of corroded glasses.

The typical activity of actinide-doped specimens ranges from ~ 0.3 to $3\text{ wt.}\%$ ²⁷. The activity of a glass doped with $1\text{ wt.}\%$ of $^{244}\text{CmO}_2$ is $\sim 6.6 \times 10^{10}\text{ Bq.cm}^{-3}$ (see section 2 in Supplementary Information). With a recoil damage volume of 300 nm^3 , it would take about 1 and 4 years for 50 and 90% of the damage volume recovery, respectively. Therefore, if a radioactive glass specimen doped with $1\text{ wt.}\%$ $^{244}\text{CmO}_2$ was leached for a short period (days to months) and then stored for about 4 years in dry storage, no signs of porosity should be observed if the radioelements were retained in the corroded layer. The dry storage time will only be about 1.3 years for a specimen doped with $3\text{ wt.}\%$ of $^{244}\text{CmO}_2$ (see Fig. 5 in Supplementary Information showing the damage evolution as a function of time). Similarly, a specimen subjected to simultaneous leaching and radiation damage may show relatively lower (or no) porosity if analysed immediately after removal from the solution compared with a non-doped specimen

subjected to the same leaching conditions. One of the implications of the irradiation-induced shrinkage in the porous SAL would be to create tensile stresses. These will effectively lead to the formation of cracks in the SAL in much the same way as mud cracks develop in clay-bearing soils upon drying²⁸ or in thin films²⁹ due to tensile stresses. Such cracks will then provide additional pathways for the water to seep in and corrode the underlying glass. Therefore, besides the differences in the degree of porosity, doped specimens would also differ from their non-doped counterparts in terms of the surface stresses and surface cracks. For the actual nuclear waste packages loaded with $\sim 16\text{ wt.}\%$ waste oxide (waste from a 33 Gwd/ton burnup PWR fuel), analysis of a short-term exposure to water (~ 100 years to simulate the accidental exposure to water) and medium-term exposure ($\sim 5000\text{--}6000$ years for the typical lifetime of the waste-package carbon-steel overpack) would be interesting. The typical activity during the first 100 years and $5000\text{--}6000$ years would be about $2 \times 10^8\text{ Bq.cm}^{-3}$ and $5 \times 10^6\text{ Bq.cm}^{-3}$ (see ref. ³⁰), respectively. At these activity levels, it would take more than 10^{10} and 5×10^{11} years for the entire glass volume to be damaged (assuming the activity values at 5000 years throughout). Therefore, the effects of self-irradiation damage on the porosity will be negligible: firstly because of the very slow/negligible recovery and secondly because the glasses will be in constant contact with water, which will nullify any slow recovery effects. The analysis essentially shows that one has to be very cautious when comparing the microstructures of highly doped corroded glasses and non-doped specimens and projecting these results onto actual waste forms. Although a more detailed analysis of true pore-size distributions is still needed, and the typical pore recovery times quoted for the doped specimens will slightly change as a result (actually decrease), the results already highlight the need to undertake microstructural characterisation of doped and corroded specimens. In any case, it is contrary to the predominant assumption that corrosion studies on doped waste packages are most realistic. It is important to point out that recent ion irradiation studies have shown that radiation damage in glasses can increase the diffusion coefficient of water (by a factor of ~ 20 ³¹) and lead to an enhancement in the rate of forward dissolution (by a factor of ~ 4 ³²). Whether mass transport through the pores plays any significant role in evaluating these factors has not been addressed yet. It is essentially the mass transport through the pores that will

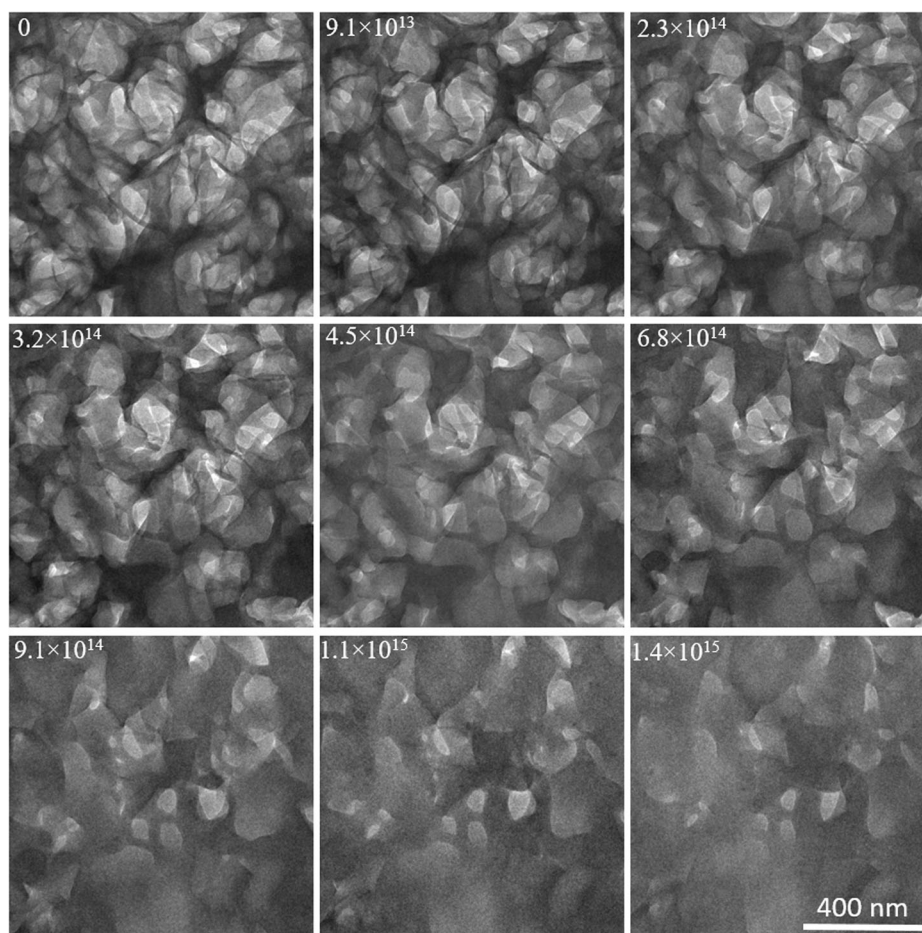


Fig. 4 BF-TEM images showing the effect of 640-keV Xe ion irradiation on the CJ8 C-S-H gel. The images are shown at different fluences starting from the undamaged specimen (fluence = 0) up to 1.4×10^{15} ions.cm⁻². The ion irradiation was performed at -130 °C.

be affected or suppressed depending on the doping concentration rather than the inter-diffusion that is primarily controlled by the damage state of the glass network. Therefore, the most realistic conditions to simulate the long-term microstructural evolution in waste packages would be to undertake corrosion studies on ion-irradiated specimens to correctly take into account the effects of radiation damage (especially depolymerisation) on the diffusion and at the same time avoid any bias that could potentially arise in highly doped specimens. Alternatively, corrosion studies could be undertaken on doped specimens that have been self-damaged over several years and now have very little residual activity left behind. It is worth mentioning that the presence of water in the pores and its impact on their closure still needs to be addressed. Although the absence or presence of water in the pores cannot be directly ascertained in this work, earlier studies on the behaviour of non-equilibrium noble gas precipitates and cavities have shown that cavities and under-pressurised precipitates shrink and close, whereas equilibrium precipitates remain stable towards ballistic collisions. Therefore, the behaviour of the pores observed here strongly suggests that they are either significantly under-pressurised or empty. This would not be surprising because water can diffuse out of the specimens during their preparation in the FIB system and under the TEM vacuum ($p \sim 8 \times 10^{-8}$ mbar). Nonetheless, due to the inherent complexity, it would perhaps be best to simulate the effects of the presence and absence of water on the behaviour of the cavities/pores to ballistic collisions using atomistic simulations. Furthermore, it is important to highlight that the recoil damage volume of 300 nm³ as assumed in the analysis above is essentially

the damage volume that exists at the end of the ballistic collisions. The actual region affected by the collision cascades during the ballistic phase can be larger than this. Therefore, the pores in radioactive waste forms may recover at a relatively faster rate than those assumed above. This issue can also be addressed by atomistic simulations by comparing the volume of the disordered region created during the ballistic phase with the damage volume used here.

In conclusion, the work reported here showed that decades of corrosion under alkaline conditions resulted in the formation of a highly porous C-S-H-type gel in the Ca-bearing CJ8 glass, whereas the Al-bearing glass reorganised into a fine nanoporous gel-like material. The microstructure of the CJ8 glass could be explained on the basis of a mechanism involving dissolution and reprecipitation, whereas the CJ2 glass microstructure is consistent with partial hydrolysis and internal reorganisation of the hydrolysed aluminosilicate glass skeleton. The results highlight that the initial glass composition plays an important role in the underlying corrosion mechanisms, and the addition of Al increases the corrosion resistance of the glasses. Therefore, any universal glass corrosion model would need to take into account the initial glass composition to address the microstructural evolution of the surface alteration layers. Irrespective of the fine microstructural details of the surface alteration layers, the porosity in both the glasses was remarkably healed by ballistic collisions causing a mass flow from the regions of high density towards the regions of low density. The results showed that ballistic collisions can lead to a different microstructure in highly doped glasses compared with the microstructure of the non-doped glasses and actual waste

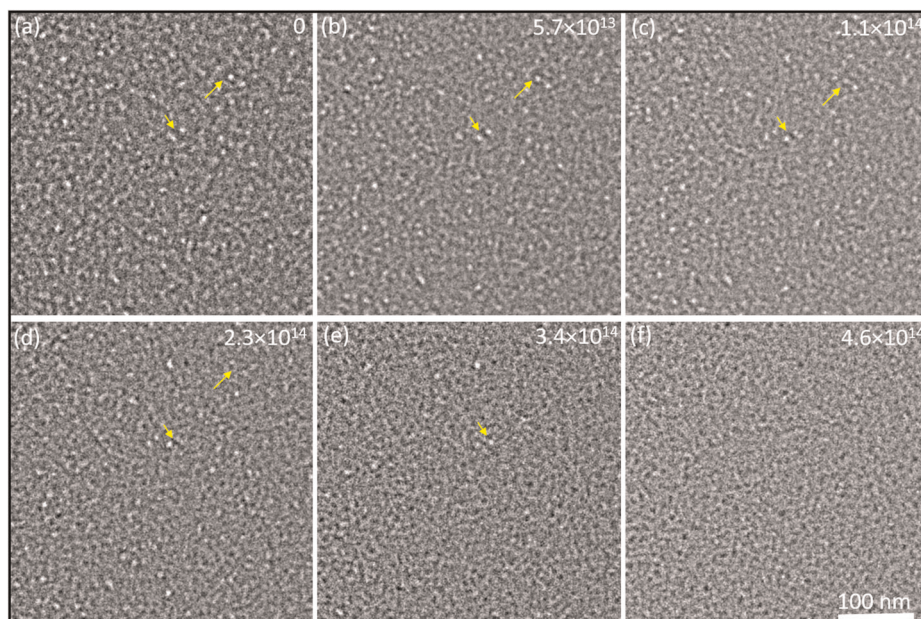


Fig. 5 BF-TEM images showing the effect of 600-keV Xe ion irradiation on the CJ2 gel. The images are shown at different fluences starting from the undamaged specimen (fluence = 0) up to 4.6×10^{14} Xe.cm⁻² at which cavities were no longer observed. The arrows indicate specific cavities at various fluences to guide the eye to demonstrate their evolution with irradiation.

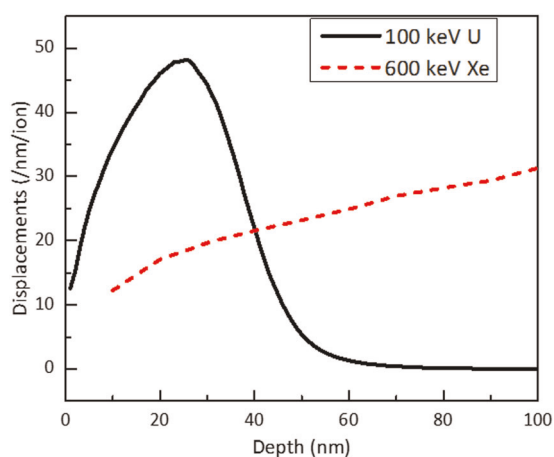


Fig. 6 Displacement damage profiles in the CJ2 glass: SRIM³⁸ predicted damage profiles (displacements per nm per ion) for 100 keV U and 600 keV Xe ions in the CJ2 glass.

packages. Although it might be assumed that corrosion of the doped glasses would best simulate the corrosion under geological conditions, the current results show that such a case is not so straightforward, and that details such as doping concentration, storage time, storage conditions and residual activity also need to be considered.

METHODS

Specimen composition and leaching of powders

Powders of CJ2 (61.22 SiO₂, 13.27 Na₂O, 18.9 B₂O₃ and 6.6 wt.% Al₂O₃) and CJ8 glasses (61.97 SiO₂, 13.42 Na₂O, 19.12 B₂O₃ and 5.49 wt.% of CaO) of 40–100- μ m size ($S/V = 80$ cm⁻¹) were leached in static mode for 7876 and 7291 days, respectively, at 90 °C and pH^{90°C} 9 (for more details see ref. ¹⁶). The pH as measured at 90 °C remained around nine, because of the buffering effect due to the release of B. The solution was regularly analysed using ICP-OES to follow the release of various elements into the solution (see Fig. 2 in the Supplementary Information). About 60% of the CJ2 glass was leached after ~7876 days of leaching, whereas 100% of the CJ8 glass

was already leached after ~6000 days of leaching. The lamellae for TEM analysis were prepared via FIB milling using 30-keV Ga ions with ion currents in the range of 1 nA to 50 pA during polishing. For leached powders, a small quantity of the powdered particles was mixed with ethanol, and then a few drops were placed on an aluminium foil to disperse the particles. The foil was placed on a standard SEM stub and coated with about 110 nm of chromium using a Quorum QT150 plasma sputter coater. The coated stub was then placed in FEI Quanta 200 3D SEM-FIB system. The TEM lamellae were made from leached particles measuring about 25 \times 40 \times 20 μ m to 40 \times 60 \times 25 μ m in *x*, *y* and *z* directions. Before making the TEM lamellae from the particles, a region of interest on the particles (usually in the centre) was deposited with carbon or Pt (20 \times 3 \times 2 μ m in *x*, *y* and *z*) to avoid any ion beam damage in this region. The particles of interest were then lifted by Omniprobe using a tungsten needle and welded onto a FIB support grid using deposited carbon. The TEM lamellae were then prepared by milling away almost equal thicknesses from either side parallel to the *xz* plane, leaving thin lamellae of ~2- μ m thickness in the middle for final polishing. These were then polished to electron transparency using the standard FIB procedure as detailed elsewhere³³.

Leaching of monoliths and ToF-SIMS (short-term leaching experiment)

Polished specimens of ~5 \times 5 \times 1.5 mm³ of the CJ8 and CJ2 glasses were leached for 33 days at 90 °C and pH^{90°C} 9. The solution was spiked with 0.012 M of ²⁹SiO₂ (²⁹Si/²⁸Si = 79, and $Q/K_{am. silica} = 0.95$). In terms of the concentration of Si and the pH, this solution is similar to that reached in the long-term experiments. The enrichment in ²⁹Si allowed the calculation of accurate mass balance for this key element. At the end of the experiment, the coupons were quickly rinsed with deionized water, dried at 30 °C and analysed by ToF-SIMS depth profiling (more information on drying is presented in section 5 in the Supplementary Information). ToF-SIMS analyses were performed by TESCAN ANALYTICS at Fuveau (France) with an IONTOF GmbH[®] TOF 5 operated in sputtering mode with two primary beams (Bi₁⁺ 25 keV, 1.5 pA and O₂⁺ 2 keV, 600 nA). The abraded area and the analysed area were 200 \times 200 μ m² and 50 \times 50 μ m², respectively. After each cycle, the surface charge was neutralised with a low-energy electron beam. At the end, the crater depth was measured by a mechanical profilometer. For more details about the application of this technique to glass alteration see ref. ³⁴. Solutions were also analysed both by ICP-OES to determine the concentrations of glass cations and MC-ICP-MS to determine the silicon isotopic ratio following the method described in ref. ³⁵.

SEM

The SEM analysis was performed on an FEI Quanta 200 3D dual-beam FIB-SEM system. For SEM imaging, the powdered particles were first mixed with ethanol, and then a few drops were placed on a standard SEM stub. After drying, these particles were sputter-coated with a thin layer of Cr (~10 nm) using a Quorum QT150 plasma sputter coater. The SEM images were captured using secondary electrons and 30-keV Ga ions (50 pA) to better capture the near-surface features.

TEM imaging and ion irradiation

Because glass specimens are sensitive to electron-beam damage, the TEM imaging was performed at a low temperature of -130°C using a 300-keV electron beam and an electron flux of less than 1.5×10^{17} electrons. cm^{-2} . s^{-1} (CJ8 at -100°C , and CJ2 at -130°C). The specimens were cooled to the desired temperature using a liquid nitrogen-cooled Gatan Model 636 holder and imaged within 2 min of switching on the electron beam to limit any damage to the cavities present in the corroded glasses. The distribution of cavities/pores in the porous regions of the specimen as recorded in the TEM images was analysed using the Fiji software³⁶ by first thresholding the images and then using the particle analysis tool to fit the pores with circles to evaluate the pore diameters. The specimen thickness was measured using EELS and energy-filtered transmission electron microscopy (EFTEM) with no objective aperture (collection angle >100 mrad, parallel beam incidence) giving values between 0.5 and 0.7 inelastic mean-free paths (this translates into 100–150 nm as discussed in the Supplementary Information). The ion irradiation was performed at the MIAMI-2 facility at the University of Huddersfield using its in situ TEM capability (Hitachi-9500 TEM)³⁷. All the ion irradiations were performed with ^{132}Xe ions at -130°C using fluxes of 4.8×10^{11} and 5.7×10^{11} ions. cm^{-2} for 600- and 640-keV ions used on CJ2 and CJ8 glasses, respectively (21-year specimens). The ion energy was chosen such that any implantation is avoided, and all the ions are transmitted through the specimen. The electron beam was switched off during the ion irradiation and only turned on after regular intervals to capture the images with each requiring only around 5 s of electron-beam exposure.

DATA AVAILABILITY

The data that support the findings of this study are available from the corresponding author upon request.

Received: 10 August 2019; Accepted: 12 March 2020;

Published online: 15 April 2020

REFERENCES

- Bunker, B. C. Molecular mechanisms for corrosion of silica and silicate glasses. *J. Non-Cryst. Solids* **179**, 300–308 (1994).
- Gin, S. et al. Origin and consequences of silicate glass passivation by surface layers. *Nat. Commun.* **6**, 6360 (2015).
- Gin, S. et al. Dynamics of self-reorganization explains passivation of silicate glasses. *Nat. Commun.* **9**, 1–9 (2018).
- Geisler, T. et al. Aqueous corrosion of borosilicate glass under acidic conditions: a new corrosion mechanism. *J. Non Cryst. Solids* **356**, 1458–1465 (2010).
- Hellmann, R. et al. Nanometre-scale evidence for interfacial dissolution-precipitation control of silicate glass corrosion. *Nat. Mater.* **14**, 307–311 (2015).
- Geisler, T., Dohmen, L., Lenting, C. & Fritzsche, M. B. K. Real-time in situ observations of reaction and transport phenomenon during silicate glass corrosion by fluid-cell Raman spectroscopy. *Nat. Mater.* **18**, 342–349 (2019).
- Perez, A. et al. Comparing the reactivity of glasses with their crystalline equivalents: the case study of plagioclase feldspar. *Geochim. Cosmochim. Acta* **254**, 122–141 (2019).
- Gin, S. et al. Atom-Probe Tomography, TEM and ToF-SIMS study of borosilicate glass alteration rim: a multiscale approach to investigating rate-limiting mechanisms. *Geochim. Cosmochim. Acta* **202**, 57–76 (2017).
- Cailleteau, C. et al. Insight into silicate-glass corrosion mechanisms. *Nat. Mater.* **7**, 978–983 (2008).
- Geisler, T. et al. Towards a unifying mechanistic model for silicate glass corrosion. *npj Mater. Degrad.* **2**, 1–10 (2018).
- Gin, S. Open scientific questions about nuclear glass corrosion, *procedia. Mater. Sci.* **7**, 163–171 (2014).
- Frugier, P., Minet, Y., Rajmohan, N., Godon, N. & Gin, S. Modeling glass corrosion with GRAAL. *npj Mater. Degrad.* **2**, 1–13 (2018).
- Gin, S. et al. An international initiative on long-term behavior of high-level nuclear waste glass. *Mater. Today* **16**, 243–248 (2013).
- Vienna, J. D., Ryan, J. V., Gin, S. & Inagaki, Y. Current understanding and remaining challenges in modeling long-term degradation of borosilicate nuclear waste glasses. *Int. J. Appl. Glas. Sci.* **4**, 283–294 (2013).
- Peuget, S., Tribet, M., Mougnaud, S., Miro, S. & Jégou, C. Radiations effects in ISG glass: from structural changes to long-term aqueous behavior. *npj Mater. Degrad.* **2**, 23 (2018).
- Gin, S., Beaudoux, X., Angéli, F., Jégou, C. & Godon, N. Effect of composition on the short-term and long-term dissolution rates of ten borosilicate glasses of increasing complexity from 3 to 30 oxides. *J. Non-Cryst. Solids* **358**, 2559–2570 (2012).
- Richardson, I. G. Tobermorite/jennite- and tobermorite/calcium hydroxide-based models for the structure of C-S-H: Applicability to hardened pastes of tricalcium silicate, β -dicalcium silicate, Portland cement, and blends of Portland cement with blast-furnace slag, metakaol. *Cem. Concr. Res.* **34**, 1733–1777 (2004).
- Kumar, A. et al. The atomic-level structure of cementitious calcium silicate hydrate. *J. Phys. Chem. C* **121**, 17188–17196 (2017).
- Groves, G. W. TEM studies of cement hydration. *MRS Proc.* **85**, 3–12 (1987).
- Sheth, N. et al. Spectroscopic ellipsometry study of thickness and porosity of the alteration layer formed on international simple glass surface in aqueous corrosion conditions. *npj Mater. Degrad.* **2**, 1–9 (2018).
- Ducasse, T. et al. Alteration of synthetic basaltic glass in silica saturated conditions: analogy with nuclear glass. *Appl. Geochem.* **97**, 19–31 (2018).
- Mir, A. H., Hinks, J. & Donnelly, S. E. Ballistic-damage-induced size changes in equilibrium and under-pressurized Xe precipitates in amorphous silica. *J. Nucl. Mater.* **519**, 229–238 (2019).
- Zhu, X. F. et al. Direct observation of irradiation-induced nanocavity shrinkage in Si. *Appl. Phys. Lett.* **79**, 3416–3418 (2001).
- Okunlewski, M. A., Ashkenazy, Y., Heuser, B. J. & Averbach, R. S. Molecular dynamics simulations of void and helium bubble stability in amorphous silicon during heavy-ion bombardment. *J. Appl. Phys.* **96**, 4181–4188 (2004).
- Maugeri, E. A. et al. Calorimetric study of glass structure modification induced by alpha decay. *J. Am. Ceram. Soc.* **7**, 1–7 (2012).
- Peuget, S. et al. Irradiation stability of R7T7-type borosilicate glass. *J. Nucl. Mater.* **354**, 1–13 (2006). Aug.
- Peuget, S., Delaye, J.-M. & Jégou, C. Specific outcomes of the research on the radiation stability of the French nuclear glass towards alpha decay accumulation. *J. Nucl. Mater.* **444**, 76–91 (2014).
- Lachenbruch, A. H. *Mechanics of Thermal Contraction Cracks and Ice-Wedge Polygons in Permafrost* (Geological Society of America, 1962).
- Xia, Z. C. & Hutchinson, J. W. Crack patterns in thin films. *J. Mech. Phys. Solids* **48**, 1107–1131 (2000).
- Mir, A. H., Monnet, I., Boizot, B., Jégou, C. & Peuget, S. Electron and electron-ion sequential irradiation of borosilicate glasses: impact of the pre-existing defects. *J. Nucl. Mater.* **489**, 91–98 (2017).
- Mougnaud, S. et al. Heavy ion radiation ageing impact on long-term glass alteration behavior. *J. Nucl. Mater.* **510**, 168–177 (2018).
- Lönartz, M. I. et al. The effect of heavy ion irradiation on the forward dissolution rate of borosilicate glasses studied in situ and real time by fluid-cell Raman spectroscopy. *Materials* **12**, 1–13 (2019).
- Mir, A. H., Hinks, J. A., Delaye, J.-M., Peuget, S. & Donnelly, S. E. Xenon solubility and formation of supercritical xenon precipitates in glasses under non-equilibrium conditions. *Sci. Rep.* **8**, 15320 (2018).
- Collin, M. et al. Structure of international simple glass and properties of passivating layer formed in circumneutral pH conditions. *npj Mater. Degrad.* **2**, 4 (2018).
- Gourgiotis, A. et al. Silicon isotope ratio measurements by inductively coupled plasma tandem mass spectrometry for alteration studies of nuclear waste glasses. *Anal. Chim. Acta* **954**, 68–76 (2017).
- Schindelin, J. et al. Fiji: an open-source platform for biological-image analysis. *Nat. Methods* **9**, 676–682 (2012).
- Greaves, G. et al. New microscope and ion accelerators for materials investigations (MIAMI-2) system at the University of Huddersfield. *Nucl. Instrum. Methods Phys. Res. Sect. A Accel. Spectrometers, Detect. Assoc. Equip.* **931**, 37–43 (2019).
- Ziegler, J. F., Ziegler, M. D. & Biersack, J. P. SRIM—the stopping and range of ions in matter (2010). *Nucl. Inst. Methods Phys. Res. B* **268**, 1818–1823 (2010).

ACKNOWLEDGEMENTS

The authors are thankful to the Engineering and Physical Sciences Research Council for funding under grants EP/E017266/1, EP/M011135/1 and EP/M028283/1. The short-term experiments and the ToF-SIMS analyses presented in this work were supported

as part of the Centre for Performance and Design of Nuclear Waste Forms and Containers, an Energy Frontier Research Centre funded by the U.S. Department of Energy (DOE), Office of Science and Basic Energy Sciences under Award #DESC001658.

AUTHOR CONTRIBUTIONS

A.H.M. wrote the paper and performed the SEM, TEM, FIB and in situ ion irradiation. A. J., S.G. and J.M.D. performed the leaching experiments and ToF-SIMS. All the authors contributed in writing and proofreading of the final paper.

COMPETING INTERESTS

The authors declare no competing interests.

ADDITIONAL INFORMATION

Supplementary information is available for this paper at <https://doi.org/10.1038/s41529-020-0115-0>.

Correspondence and requests for materials should be addressed to A.H.M.

Reprints and permission information is available at <http://www.nature.com/reprints>

Publisher's note Springer Nature remains neutral with regard to jurisdictional claims in published maps and institutional affiliations.



Open Access This article is licensed under a Creative Commons Attribution 4.0 International License, which permits use, sharing, adaptation, distribution and reproduction in any medium or format, as long as you give appropriate credit to the original author(s) and the source, provide a link to the Creative Commons license, and indicate if changes were made. The images or other third party material in this article are included in the article's Creative Commons license, unless indicated otherwise in a credit line to the material. If material is not included in the article's Creative Commons license and your intended use is not permitted by statutory regulation or exceeds the permitted use, you will need to obtain permission directly from the copyright holder. To view a copy of this license, visit <http://creativecommons.org/licenses/by/4.0/>.

© The Author(s) 2020